



# A hybrid deterministic and stochastic approach for tsunami hazard assessment in Iquique, Chile

Juan González, et al. *[full author details at the end of the article]*

Received: 19 December 2018 / Accepted: 29 September 2019  
© Springer Nature B.V. 2019

## Abstract

The southern Peru and northern Chile coastal region is an active subduction zone that contains one of the most significant seismic gaps in the eastern Pacific basin ( $\sim 17^{\circ}\text{S}$ – $24^{\circ}\text{S}$ ). Although the gap was partially filled by the 2014  $M_w$  8.1 Iquique earthquake, there is still a high seismogenic potential to release a  $M_w$   $\sim 9$  earthquake in the near future; therefore, all the near-field coastal cities in the region face a latent tsunami threat. In this article, we propose a hybrid deterministic–stochastic multi-scenario approach to assess the current tsunami hazard level in the city of Iquique, an important commercial and industrial center of northern Chile that is home to 184,000 inhabitants. In our approach, we defined 400 stochastic, 10 deterministic and 10 homogeneous tsunamigenic earthquake scenarios, covering the entire area of the seismic gap. Based on the regional distribution of gravity anomalies and published interseismic coupling distributions, we interpreted the occurrence of four major asperities in the subduction interface of the seismic gap. The asperity pattern was used to construct a group of deterministic slip-deficit earthquake sources with seismic magnitudes ranging between  $M_w$  8.4 and  $M_w$  8.9. Additionally, we constructed 10 homogeneous slip scenarios to generate an inundation baseline for the tsunami hazard. Subsequently, following a stochastic scheme, we implemented a Karhunen–Loève expansion to generate 400 stochastic earthquake scenarios within the same magnitude range as the deterministic slip-deficit sources. All sources were used as earthquake scenarios to simulate the tsunami propagation and inundation by means of a non-hydrostatic model (Neowave 2D) with a classical nesting scheme for the city of Iquique. We obtained high-resolution data for flow depth, coastal surface currents and sea level elevation. The results suggest that the peak slip location and shelf resonance play an important role in the calculated coastal flow depths. The analysis of the entire set of simulated stochastic earthquake scenarios indicates that the worst-case scenario for Iquique is a  $M_w$  8.9 earthquake. This scenario presented a tsunami arrival time of  $\sim 12$  min, which is critical for the evacuation process. In addition, the maximum wave height and tsunami flow depth were found to be  $\sim 10$  m and  $\sim 24$  m, respectively. The observed coastal resonance processes exhibit at least three destructive tsunami wave trains. Based on historical and instrumental catalog statistics, the recurrence time of the credible worst-case earthquake scenario for Iquique ( $M_w$  8.9) is 395 years, with a probability of occurrence of  $\sim 11.86\%$  in the next 50 years.

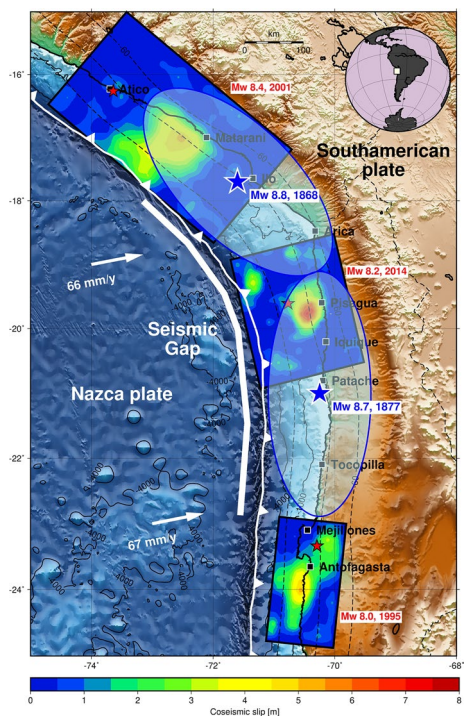
**Electronic supplementary material** The online version of this article (<https://doi.org/10.1007/s11069-019-03809-8>) contains supplementary material, which is available to authorized users.

**Keywords** Earthquake scenarios · Tsunami hazard assessment · Southern Peru · Northern Chile

## 1 Introduction

The coastal region of southern Peru and northern Chile, extending between 17°S and 24°S, is located in the active subduction zone formed by the convergence of the Nazca and South American plates (Fig. 1). The segment has been recognized as one of the most significant seismic gaps in the eastern Pacific basin (Comte and Pardo 1991; Kelleher 1972; McCann et al. 1979; Nishenko 1985). It has undergone a prolonged seismic quiescence since the two last large historical earthquakes occurred in southern Peru ( $M_w$  8.8, 1868) and northern Chile ( $M_w$  8.7, 1877). Detailed descriptions of the 1868 event reported an extended tsunami impact along more than 4000 km of the coast between Trujillo, Peru, and Chiloe Island, Chile (Soloviev and Go 1975). In northern Chile, the tsunami severely impacted the city of Arica, where tsunami wave heights of ~18 m were reported (Soloviev and Go 1975). The tsunami caused by the 1877 earthquake destroyed many cities in northern Chile, including Arica, Iquique, Cobija and Mejillones. Historical reports mention tsunami waves heights of ~20 m in Mejillones harbor (Milne 1880; Soloviev and Go 1975; Vidal Gormaz 1878). More recently, the southern Peru and northern Chile seismic gap has been affected by moderate earthquakes, including the  $M_w$  8.1 Antofagasta earthquake in 1995, the  $M_w$  8.4 Arequipa earthquake in 2001, the  $M_w$  7.7 Tocopilla earthquake in 2007 and the  $M_w$  8.2 Iquique earthquake in 2014 (Delouis et al. 1997; Hayes et al. 2014; Peyrat et al.

**Fig. 1** Tectonic framework of the southern Peru and northern Chile seismic gap. Blue ellipses indicate the historical tsunamigenic earthquakes of 1868,  $M_w$  8.8 and 1877,  $M_w$  8.7. The coseismic slip distributions of moderate earthquakes ( $M_w > 8$ ) are taken from Hayes (2017)



2010; Ruiz and Madariaga 2018; Schurr et al. 2014; Tavera et al. 2002). The 1995 Antofagasta, 2001 Arequipa and 2014 Iquique earthquakes generated moderate tsunamis (An and Liu 2014; Catalán et al. 2015; Guibourg et al. 1997; Okal et al. 2002).

Several authors have reported that the seismic gap of southern Peru and northern Chile has the potential to generate an earthquake of up to  $M_w \sim 8.9$  in the near future (Hayes et al. 2014; Métois et al. 2013; Schurr et al. 2014; Seno 2014; Villegas-Lanza et al. 2016; Ye et al. 2018). Therefore, we can infer that a serious tsunami threat exists for all the coastal cities of southern Peru and northern Chile (Okal et al. 2006). Given this condition, this article proposes a methodology to estimate tsunami hazard using a multi-scenario approach. We consider multiple seismogenic sources, which can totally or partially fill the seismic gap. In order to define the earthquake scenarios, a hybrid deterministic–stochastic scheme was designed. In this approach, we assume that large tsunamis are generated by  $M_w \geq 8.0$  earthquakes, whose locations and slip distributions on the causative fault are physically controlled by the frictional properties of the interplate contact, e.g., shear stress. The implicit idea of this assumption is that large earthquakes can represent the failure of a single asperity or a collection of two or more large asperities (Scholz and Campos 2012). We have defined a set of  $\sim 400$  earthquake scenarios, which include stochastic variability of the slip distribution in a predefined framework of asperities. The earthquake scenarios are used as the initial condition assuming instantaneous deformation for tsunami simulation to estimate coastal impacts via parameters that include wave height, inland inundation area flow depth pattern, arrival time and spectral energy. The results obtained from the proposed methodology are used to estimate the state of tsunami hazard in the city of Iquique, the site of well-documented tsunami damage resulting from the 1868 and 1877 earthquakes.

## 2 Methodological approach

### 2.1 Earthquake scenarios

To provide deterministic tsunamigenic earthquake scenarios in the southern Peru and northern Chile seismic gap, we implemented a scheme for identifying the presence of major asperities, which can control the occurrence of future earthquakes. The locations of major asperities were inferred using a combination of trench-parallel gravity anomaly (TPGA), trench-parallel topography anomaly (TPTA) and available geodetic locking models. The spatial distribution of fault locking was used to estimate the slip deficit stored in the seismic gap since the 1868  $M_w$  8.8 earthquake in southern Peru and since the 1877  $M_w$  8.7 earthquake in northern Chile. The slip deficit was calculated using the convergence velocity model GEODVEL (Argus et al. 2010); it fluctuated between 65.3 and 67.3 mm/year. This deterministic approach allowed tsunamigenic earthquake scenarios to be constructed. However, if we compare the dimensions of the maximum rupture area and the peak slip of the deterministic earthquake sources with realistic earthquakes extracted from a worldwide finite fault model database (Mai and Thingbaijam 2014), we obtain great differences (Fig. 2). In general, the deterministic earthquake sources have a lower peak slip than measured earthquakes; therefore, the deterministic approach can underestimate the tsunami parameters (Mueller et al. 2015). Thus, in a subsequent stage we calculated a large set of stochastic seismic scenarios with the slip distribution scaled to the moment magnitude.

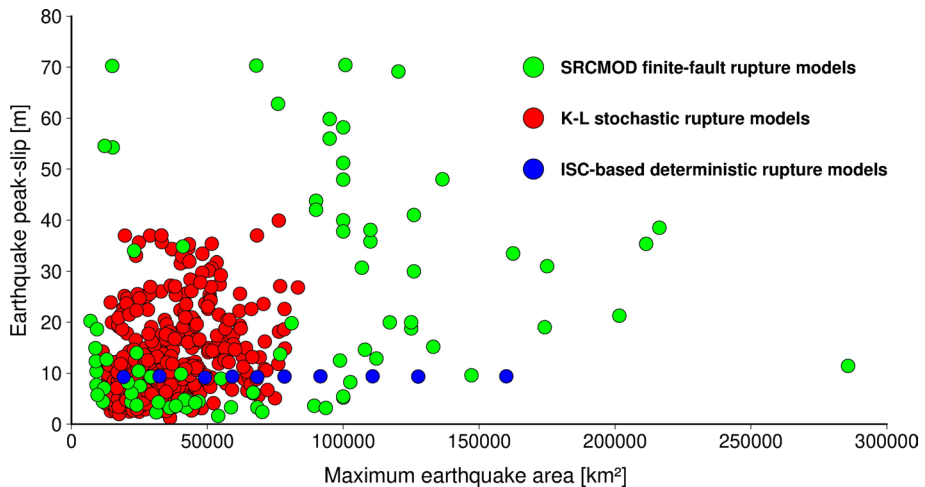


**Fig. 2** Maximum earthquake area versus peak slip of worldwide finite fault rupture models extracted from SRCMOD database (Mai and Thingbaijam 2014) contrasted with interseismic coupling (ISC)-based and Karhunen–Løve (K–L) stochastic rupture patterns estimated by the multi-scenario tsunami hazard assessment approach

Large-amplitude negative TPGAs and TPTAs observed in the forearc region can be used as a proxy to evaluate the nucleation of earthquakes in the megathrust (Song and Simons 2003). These anomalies are usually used to infer the shear traction distribution in the interplate contact (Fletcher et al. 2001; Song and Simons 2003). A strong negative anomaly is related to relatively high shear tractions and vice versa. Under this paradigm, the shear traction controls the forearc topography, gravity patterns and, indirectly, the rupture areas of large earthquakes (Song and Simons 2003). The regional distribution of anomalies in the Nazca–South American subduction zone was calculated over 377 down-dip profiles projected on the fault contact geometry given by the Slab1.0 model (Hayes et al. 2012). The profiles extend from southern Peru ( $\sim 14^{\circ}\text{S}$ ) to the Chile Triple Junction ( $\sim 45^{\circ}\text{S}$ ). As an input to calculate the gravity and topography anomalies, we used the global marine free-air gravity of Sandwell et al. (2014) and the GEBCO world bathymetric model (The General Bathymetric Chart of the Oceans, Weatherall et al. 2015), respectively (Figures S1 and S2, Supplementary material).

The geodetic locking can be defined as the ratio between the slip rate on the megathrust fault during an interseismic period and the plate convergence velocity (Chlieh et al. 2011; Métois et al. 2016). We assume that areas governed by a high degree of locking correlate with the locations of asperities, whereas areas of reduced locking could represent barriers to earthquake propagation. To characterize these two elements, we used a published interplate locking model for the region extending from  $\sim 17^{\circ}\text{S}$  in southern Peru to  $\sim 24^{\circ}\text{S}$  in northern Chile (Métois et al. 2016).

Other authors have demonstrated that the spatial distribution of slip and the rupture complexity in a given earthquake constitute a first-order control on the hydrodynamic processes and coastal impacts of tsunamis (Geist 1998; Geist and Dmowska 1999; Mueller et al. 2015). For tsunami hazard assessment, the spatial distribution of the slip of historical or future megathrust earthquakes is complex (Mueller et al. 2015); thus, as standard practice numerical models utilize a preliminary homogeneous slip distribution estimated



from scaling laws (Allen and Hayes 2017; Blaser et al. 2010). To address this complexity, LeVeque et al. (2016) implemented a stochastic method using the Karhunen–Loève (K–L) expansion to generate static hypothetical rupture scenarios with non-uniform slip patterns. Subsequently, Melgar et al. (2016) extended this method to include kinematic rupture parameters and a 3D slab model. This new method was used to generate synthetic seismic waveforms to test the earthquake early warning (EEW) system in the Cascadia subduction zone (Melgar et al. 2016). We used this methodology to distribute the slip in the segmentation generated by the deterministic approach previously detailed in this section. The megathrust area of the southern Peru–northern Chile seismic gap was simulated using the geometry of the Slab 1.0 model (Hayes et al. 2012), which was discretized into 400 subfault elements. Following the findings of Li et al. (2016), each square subfault has size of 20 km per side to efficiently capture the rupture complexity of near-field region. We constructed the geometry of a particular scenario using a random subfault of the discretized space as a central locus to define an involved rupture area based on scaling laws proposed by Blaser et al. (2010). Subsequently, to define the statistics of the slip distribution, we assumed a normal slip distribution on each subfault, including a mean ( $\mu_k$ ) and standard deviation ( $\sigma_k$ ). Under this assumption, we defined a vector as containing a normally distributed slip that was characterized by a mean vector ( $\mu$ ) and a covariance matrix ( $\hat{C}$ ) that was nominally defined as a fraction of the mean slip and an interfault correlation function ( $C_{ij}$ ), which controls the spatial statistics of slip (Melgar et al. 2016). The covariance matrix ( $\hat{C}$ ) can be expressed in terms of eigenvalues ( $\lambda_k$ ) and eigenvectors ( $v_k$ ) (LeVeque et al. 2016); finally, the K–L expansion described the slip vector  $s$  as:

$$s = \mu + \sum_{k=1}^N z_k \sqrt{\lambda_k} v_k \quad (1)$$

where the  $z_k$  are normal random numbers with mean 0 and standard deviation 1.

As noted by Melgar et al. (2016), a potential weakness of this approach is the occurrence of negative values in calculated slip distributions of stochastic rupture scenarios. To solve this issue, LeVeque et al. (2016) propose an exponentiation of the slip vector  $s$  (Eq. 1) to produce a lognormal distribution, to assure a positive slip pattern. As example for our results, we plot the histograms of slip on each subfault from the 400 realizations, showing a reasonable fit with the theoretical marginal lognormal distribution (Figs. 3, S3, S4, S5 and S6). According to LeVeque et al. (2016), a large number of samples/scenarios (e.g., 20,000) are required to explore the statistical behavior of the K–L method. It is technically unfeasible to simulate this number of scenarios for high-resolution tsunami modeling. To define a minimum optimal number of stochastic scenarios, we used Welch's  $t$  test (Welch 1951). The  $t$  test checks if two populations have an equal mean. The slip distribution of the target population (20,000 scenarios) was compared with populations of 200, 300, 400, 1000, 2000, 5000 and 10,000 scenarios, indicating that a minimum of 400 scenarios is required to represent the statistical variability of the target population (Table 1). In addition, we performed a coefficient of variation analysis (Li et al. 2016), to support the selection of a minimum number of scenarios (Table 2).

The target magnitude was previously defined by the rupture area based on the deterministic approach. The target magnitudes range between  $M_w$  8.3 and  $M_w$  8.9 and are distributed among 0.06 magnitude bins. Following the methodology of Melgar et al. (2016), we constructed 40 scenarios per magnitude bin to complete 400 events and reach the minimum number of scenarios. To avoid unrealistically large amounts of slip that are sometimes

**Fig. 3** Examples of histograms (blue) and marginal lognormal theoretical distribution with a  $\mu=0$  and  $\sigma=1$  (red) of slip on selected subfault 050, 125, 251 and 347 (orange) from the 400 stochastic realizations. The fault geometry of earthquake scenario is denoted in green and limited by the magenta polygon

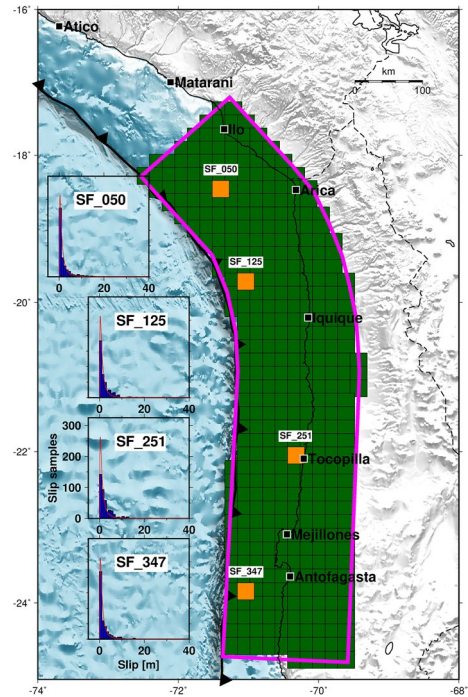


**Table 1** Summary statistical parameters of  $t$  test analysis for stochastic scenarios

Number of stochastic scenarios	Hypothesis test result <sup>a</sup>	$p$ value
200	1	<0.01
300	1	<0.01
400	0	0.54
1000	1	<0.01
2000	1	<0.01
5000	0	0.68
10,000	0	0.07
20,000	0	1

<sup>a</sup>1, reject the null hypothesis that the data comes from normal distributions with equal means and equal unknown variances at the 5% of significance level; 0 otherwise

observed in stochastic scenarios, initially we use the deterministic approach to propose a baseline peak slip value based on the geodetic slip deficit of  $\sim 10$  m since the 1877  $M_w$  8.7 event (Métois et al. 2016). Nevertheless, knowledge of the seismogenic behavior of the Chile–Peru seismic gap is restricted to a short time span of 500 years before the present (Comte and Pardo 1991; Lomnitz 2004), and it is unknown if the last large event in 1877 released all the slip deficits previously stored in the subduction zone. On the other hand, recent tsunamigenic earthquakes— $M_w$  9.2 Sumatra in 2004 (Chlieh et al. 2007; Piatanesi and Lorito 2007);  $M_w$  8.8 Chile in 2010 (Lorito et al. 2011; Vigny et al. 2011); and  $M_w$  9.0 Japan in 2011 (Pollitz et al. 2011; Simons et al. 2011)—have presented peak slip zones

**Table 2** Summary statistical parameters of coefficient of variance (CoV) analysis for stochastic scenarios

Number of stochastic scenarios	Coefficient of variation (CoV)
200	1.44
300	1.45
400	1.48
1000	1.44
2000	1.43
5000	1.44
10,000	1.45
20,000	1.45

of 20 m, partially uncorrelated with high slip-deficit segments. Therefore, following the criteria used to balance the scenario variability and current tectonic knowledge of subduction zones presented by Melgar et al. (2016) and taking into account our deterministic slip-deficit baseline, we set the maximum peak slip in stochastic source simulations to 40 m.

## 2.2 Tsunami modeling

As mentioned earlier, the fault geometry in this work (e.g., slab depth, strike and dip) follows the Slab1.0 model (Hayes et al. 2012). For tsunami models, the rake angle of slip vector at the earthquake source is calculated using the mathematical relationship proposed by Michael (1990):

$$\lambda = \tan^{-1} \left[ \frac{\tan(\theta)}{\cos \phi} \right] \quad (2)$$

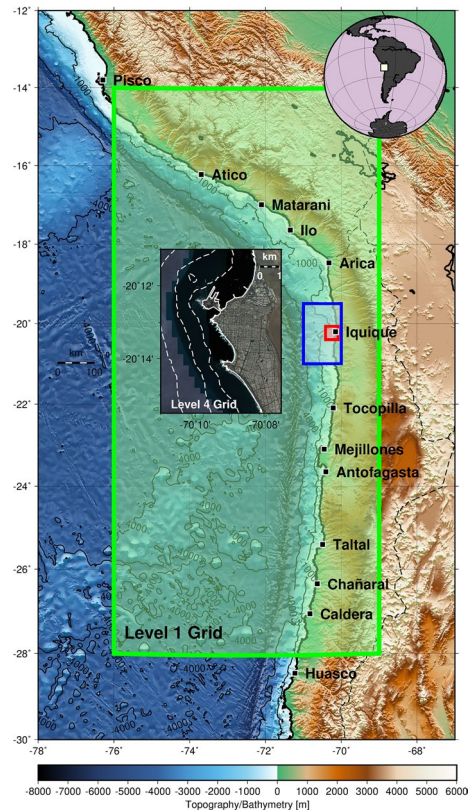
where  $\theta$  is the convergence direction with respect to the fault strike and  $\phi$  is dip of the fault.

For the tsunami modeling, the down-dip limit of the seismogenic zone was constrained to a depth of ~70 km based on the available locking model (Métóis et al. 2016). A down-dip boundary located between a depth of 40 and 50 km was proposed based on previous analysis of moderate earthquakes (Béjar-Pizarro et al. 2010; Sobiesiak et al. 2007) and thermal modeling (Oleskevich et al. 1999). In order to maintain a reasonable scale relationship among magnitude, rupture area and peak slip, we selected a deeper down-dip limit. The subduction fault was divided into subfault elements 20 km wide and long in agreement with the criteria proposed by Li et al. (2016) to improve the accuracy and decrease the dispersion effects of tsunami scenario modeling and achieve a reasonable computation time.

High-resolution tsunami numerical simulations were performed using the Non-hydrostatic Evolution of Ocean WAVEs model (NEOWAVE, Yamazaki et al. 2011). NEOWAVE is a two-dimensional, depth-integrated and non-hydrostatic model designed to describe dispersive waves and cope with flow discontinuities generated in hydraulic jumps, breaking waves and bores (Yamazaki et al. 2011). This model has recently been applied to analyze the generation, propagation and inundation processes of both far- and near-field tsunamis (Bai et al. 2014; Cheung et al. 2013; Lay et al. 2013; Yamazaki et al. 2013) and used for probabilistic design of coastal infrastructure (Cheung et al. 2011), shelf resonance analysis (Yamazaki and Cheung 2011) and post-tsunami surveys (Catalán et al. 2015; Aránguiz et al. 2016).

For precise calculation of inundation/runup processes, we set up four levels of nested grids for near-field tsunami scenarios. The level 1 grid, with a resolution of 2 arcmin ( $\sim 3600$  m), extended from central Peru ( $\sim 14^\circ\text{S}$ ) to central Chile ( $\sim 28^\circ\text{S}$ ), solving the seafloor deformation and near-field tsunami propagation along coastline. The level 2 grid, with a resolution of 30 arcsec ( $\sim 900$  m), and level 3 grid, with a resolution of 6 arcsec ( $\sim 180$  m), described the local scale of potential shelf and slope resonance of tsunami waves. The level 4 grid, with a resolution of 1 arcsec ( $\sim 30$  m), covered the coastal settlement of Iquique ( $\sim 20^\circ\text{S}$ ). Results from this grid level were used to analyze the local variability of runup/inundation processes along the coastline. In addition, sea surface elevation, currents and spectral energy data from a synthetic tide gauge were analyzed. The level 1 and level 2 grids were extracted from the GEBCO world bathymetric model (Weatherall et al. 2015), the level 3 grids were constructed using regional nautical charts and SRTM (Shuttle Radar Topography Mission) data (Farr et al. 2007), and the level 4 grid was generated using local nautical charts combined with detailed bathymetry provided by the Ministry of Public Works and high-resolution LIDAR topography provided by the JICA-SATREPS project (Fig. 4). The topographic, bathymetric and coastline data were filtered, blended and gridded using computing algorithms of Generic Mapping Tools (GMT) (Smith and Wessel 1990; Wessel and Smith 2013). The simulations covered an elapsed time of 4 h, with computation time steps of 1, 0.5, 0.25 and 0.125 s for grids 1, 2, 3 and 4, respectively. The Manning's roughness coefficient was defined as 0.025, which is typical for ocean bottom.

**Fig. 4** Nested grid setup and bathymetric data used for the modeling of near-field tsunami scenarios in the southern Peru and northern Chile seismic gap. The level 1 grid is highlighted by the green rectangle. The level 2 and 3 grids are shown in the blue and red rectangles, respectively. For the level 4 grid, we show the bathymetric contours (dashed lines) every 25 m of water depth gridded from local nautical charts



Spectral analysis of simulated tsunami waveforms was performed by a fast Fourier transform (FFT) algorithm (Frigo and Johnson 1998; Heidarzadeh and Satake 2014; Heidarzadeh et al. 2015). The FFT technique was applied for an elapsed time of 4 h in numerical simulation, with a modeling time window aimed at optimizing the computation time of all scenarios. The purpose of FFT is to characterize the spectral energy peaks associated with the seismic source and coastal resonance effects.

## 2.3 Probabilistic earthquake recurrence

The probabilistic earthquake recurrence assessment was developed to estimate the return period of the credible worst-case tsunamigenic scenario for the city of Iquique, located in the southern Peru and northern Chile seismic gap.

The estimation of earthquake recurrence time is not an easy task and is usually considered as one of the main sources of uncertainty in seismic and tsunami hazard assessment. We estimated the recurrence times of large megathrust earthquake scenarios using the Gutenberg–Richter relationship (Gutenberg and Richter 1944). First, we used a homogenized catalog in terms of moment magnitude based on an improved error-corrected method for the northern Chile zone (Das et al. 2018). The catalog includes historical and instrumental recorded events until 2016. A filtered subset of interplate seismicity was selected within the expected rupture polygon. The seismic parameters such as the  $b$ -value and earthquake recurrence rates were obtained from the Gutenberg–Richter relationship by means of the maximum likelihood methodology proposed by Weichert (1980). The Aki–Utsu estimator methodology from Kijko and Smit (2012) has been used to appraise the recurrence and the probabilities of occurrence of a range of magnitudes following the probability density function (Aki 1965):

$$f(m; \beta) = \beta e^{[-\beta(m-M_{\min})]} \quad \text{for } m \geq M_{\min} \quad (3)$$

The Gutenberg–Richter relationship normally considers the completeness above a given earthquake magnitude ( $M_{\min}$ ) and an upper magnitude limit ( $M_{\max}$ ). This upper limit was constrained by the expected maximum credible scenario magnitude ( $M_w$  8.9), which is assumed to completely fill the seismic gap of southern Peru and northern Chile. However, due to the uncertainty of this maximum credible scenario, we prefer a more conservative approach, assuming a magnitude  $M_w$  9.1 earthquake, as has been proposed in other studies (Ye et al. 2018).

## 3 Results

### 3.1 Deterministic earthquake scenarios

The analysis of two large-amplitude TPGAs and TPTAs suggests two segments with high shear traction in the seismic gap of southern Peru and northern Chile, which are interpreted as highly coupled zones (see Fig. 5a, b). One segment extends between Ilo and Pisagua ( $\sim 18^\circ\text{S}$ – $\sim 20^\circ\text{S}$ ); it is limited along-strike by the ruptures of the 2001  $M_w$  8.4 Arequipa earthquake (Ruegg et al. 2001) and the 2014  $M_w$  8.1 Iquique earthquake (Schurr et al. 2014). A second segment is located near the trench from Patache to the Mejillones Peninsula ( $\sim 21^\circ\text{S}$ – $\sim 23^\circ\text{S}$ ); it is limited along-strike by the 2014  $M_w$  8.1 Iquique earthquake and the 1995  $M_w$  8.0 Antofagasta earthquake (Delouis et al. 1997). Recent geodetic

**Fig. 5** Geophysical parameters of southern Peru and northern Chile seismic gap. **a** Trench-parallel gravity anomaly, **b** trench-parallel topography anomaly, **c** interseismic coupling and **d** instrumental and historical seismicity catalog provided by Das et al. (2018)

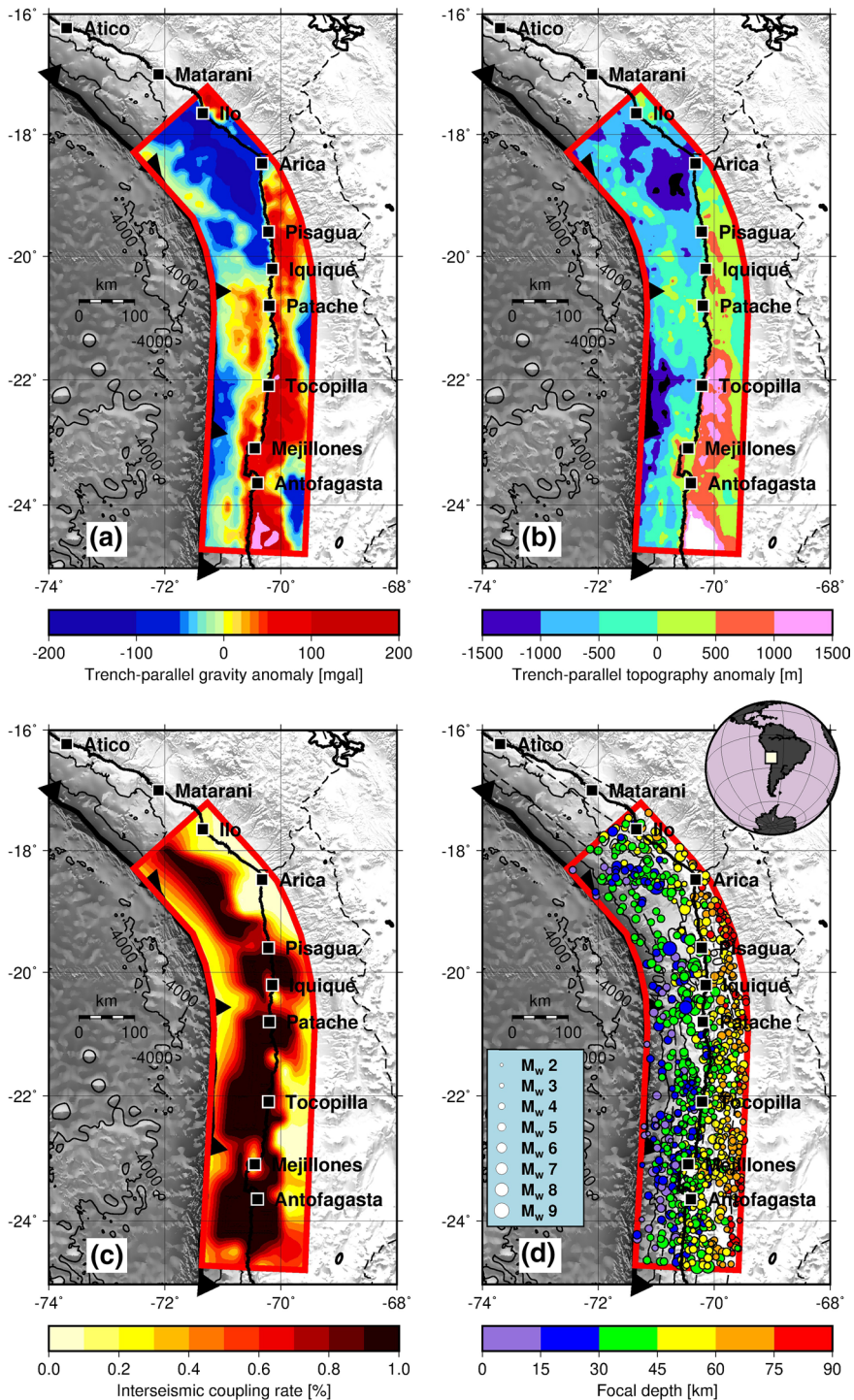
observations of the afterslip processes of the  $M_w$  8.1 Iquique earthquake reinforced the idea of a seismotectonic barrier located at  $\sim 21^\circ\text{S}$  (Hoffmann et al. 2018; Shrivastava et al. 2019). This segmentation can also be inferred based on available interseismic locking models (Chlieh et al. 2011; Métois et al. 2016) (see Fig. 5c). The instrumental and historical earthquake catalog provided by Das et al. (2018) shows a seismic quiescence in both segments, indicating a significant stress budget stored since the last major tsunamigenic earthquakes in 1868 and 1877 (see Fig. 5d). As a result, we obtained the geographical locations of four higher slip-deficit zones extending from  $\sim 18^\circ\text{S}$  to  $\sim 24^\circ\text{S}$  that can be interpreted as major remaining seismic asperities. Subsequently, the deterministic scenarios described in Sect. 2.1 were constructed by combining one or more asperities to generate ten plausible deterministic tsunami scenarios. The moment magnitudes range from  $M_w$  8.4 to  $M_w$  8.9 (Fig. 6 and Table S1).

### 3.2 Stochastic earthquake scenarios

Based on the geometry of the deterministic worst-case scenario (scenario 10,  $M_w$  8.9, see Fig. 6), we generated 400 hypothetical earthquake rupture scenarios with a geologically constrained stochastic slip pattern supported by K–L expansion as outlined in LeVeque et al. (2016) and Melgar et al. (2016). In addition to the variable slip of non-uniform scenarios, we also observed variations around the mean length and width following the scaling law of Blaser et al. (2010), associated with estimated magnitudes. A brief overview of the distribution of sizes and magnitudes for the stochastic scenarios is presented in Fig. 7. In all these scenarios, we observed a reasonable fit with the selected scaling relationship. The rupture width of these scenarios did not present a saturation process, which is normally associated with the down-dip selection criterion, improving the moment magnitude calculation. Like Melgar et al. (2016), we observed a discrepancy between the target and actual moment magnitudes, which generated a more extended magnitude variation that ranges between  $M_w$  8.0 and 9.1. Subsequently, we defined a stochastic worst-case tsunami scenario as the stochastic earthquake capable of generating the maximum flow depth at a specific coastal site in northern Chile.

Although our stochastic rupture scenario database consisted of a finite number of realizations ( $\sim 400$ ), they are useful for progressing toward a comprehensive understanding of the relationship between physical processes of the rupture and the tsunami parameters. Previous works based on numerical and physical tsunami modeling (Plafker 1997; Rosenau et al. 2010; Ruiz et al. 2015) have shown a positive correlation between the maximum flow depth/runup and the increase in peak slip at the seismic source in a non-breaking wave regime. We observed a similar correlation pattern in some particular rupture scenarios; for example, two scenarios proposed for Iquique have an identical magnitude ( $M_w$  8.88), but different peak slip locations and values, causing a disparity in flow depth estimation (Fig. 8; Table S2). Meanwhile, we expected a high tsunami runup at coastal sites using a specific source such as scenario 331 ( $M_w$  8.86), which nucleated in a reduced along-strike section of the seismogenic zone (an effective length of  $\sim 350$  km), but the constrained peak slip value was high ( $\sim 34$  m). However, the regression relationship between peak slip and the maximum flow depth based on all





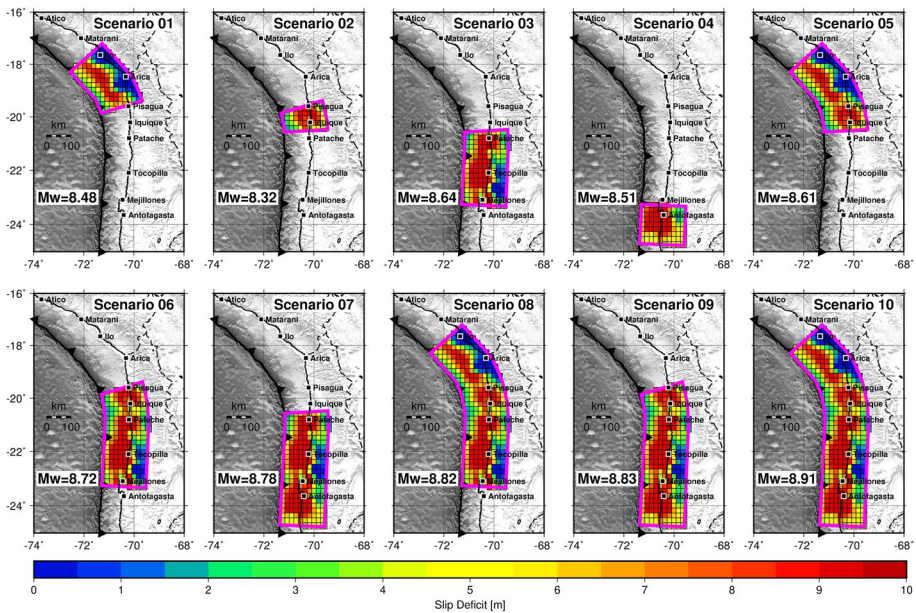


**Fig. 6** Deterministic seismic scenarios based on geodetic slip deficit in southern Peru and northern Chile seismic gap

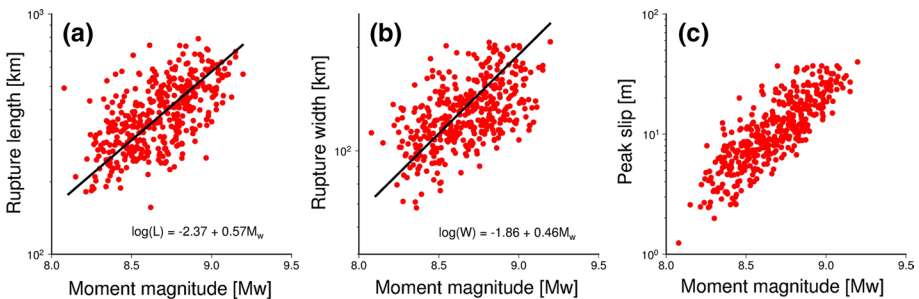


**Fig. 7** Statistical parameters for K–L expansion stochastic scenarios, including a comparison with scaling laws proposed by Blaser et al. (2010). **a** Moment magnitude ( $M_w$ ) versus maximum rupture length, **b**  $M_w$  versus maximum width length, **c**  $M_w$  versus peak slip

the stochastic models suggested a weak correlation ( $r=0.22$ ), associated with the use of a wave breaking regime for the tsunami simulations. The same poor correlation was observed between the moment magnitude and the maximum flow depth ( $r=0.26$ ) of the stochastic rupture scenarios (Fig. 9).

The maximum flow depth obtained from the deterministic tsunami scenarios was clearly underestimated in comparison with that obtained from stochastic sources (Fig. 9). The underestimation probably resulted from the low peak slip calculation caused by the smoothness included in the interseismic coupling models. The reported flow depths of historical tsunamigenic earthquakes in the seismic gap (Soloviev and Go 1975) fit reasonably well with the stochastic rupture scenarios, but we observed high

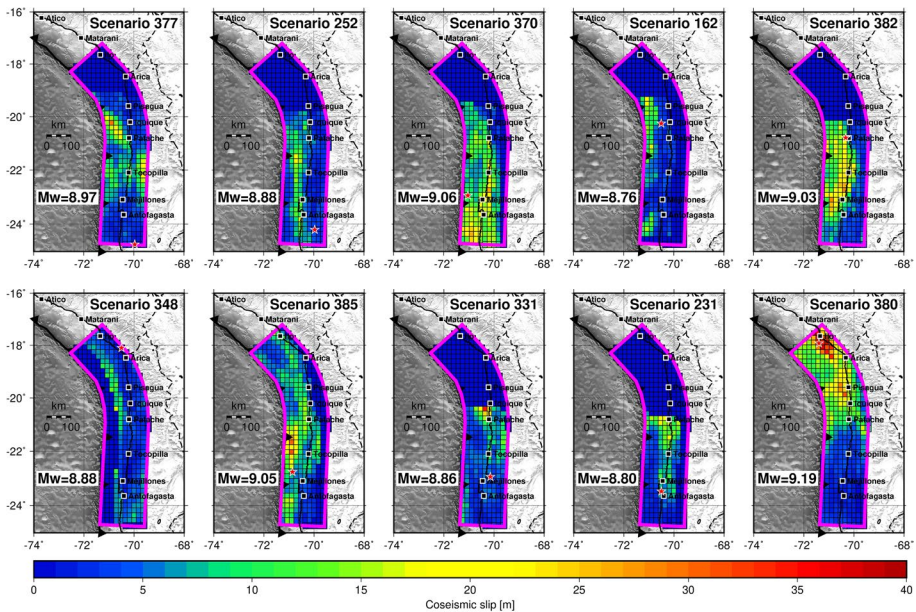


**Fig. 8** Examples of megathrust earthquake scenarios based on the stochastic technique of K–L expansion

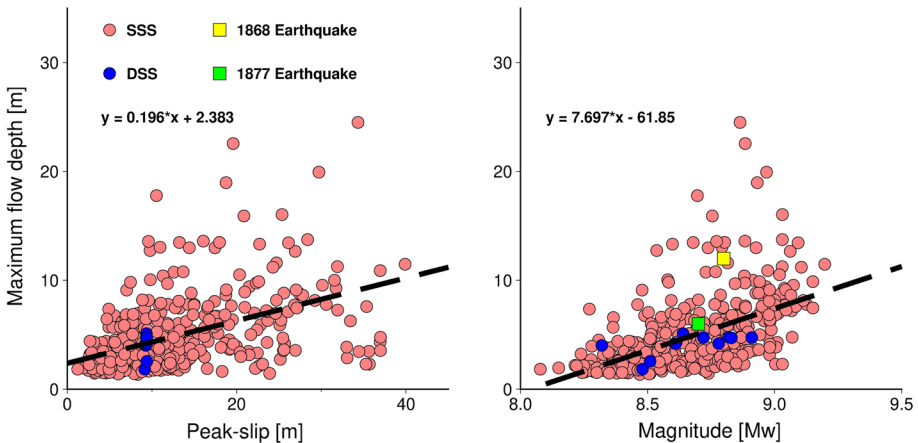


**Fig. 9** Near-field modeled maximum flow depth versus peak slip and calculated moment magnitude ( $M_w$ ) of stochastic seismic scenarios (SSS) and deterministic seismic scenarios (DSS) in the city of Iquique

variability in the results (Fig. 9). The peak slip magnitude can be a first-order control on the maximum flow depth on the coastline, but the high variability may be associated with other secondary factors such as edge waves, shelf resonance and other local effects related to coastal geomorphology (e.g., Catalán et al. 2015; Cheung et al. 2013; Melgar and Ruiz-Angulo 2018; Yamazaki et al. 2013).



### 3.3 Case study: tsunami modeling of credible worst-case scenario

To test the results of the stochastic scenarios, we carried out a detailed analysis of tsunami hazard in the city of Iquique (70°09'W; 20°13'S), which was selected as a case study due to the major damage caused by the earthquakes of 1868 and 1877, as well as the significant tsunami hazard exposure of its inhabitants (~184,000) and critical coastal infrastructure associated with its intense touristic, port and industrial activities (Aguirre et al. 2018).

We previously defined the credible worst-case scenario as a stochastic earthquake that produces a maximum flow depth at a specific site. In Iquique, the maximum flow depth of 24.51 m is associated with stochastic scenario 377 ( $M_w$  8.9). In the middle of the seismic gap, the credible worst-case scenario simulated for Iquique presents an extensive inundation of developed areas, reaching a total area of 5.86 km<sup>2</sup>. In the northern section of the city, we notice a maximum tsunami intrusion of ~1.30 km with a flow depth varying between ~8 and 12 m, affecting the local business district. The area encompassing the port facilities, historical downtown and tourist zone exhibits a maximum horizontal inundation of ~1.27 km with a flow depth ranging from 9.70 to 15.55 m. Between Cavancha Cove and Brava Beach, the maximum runup estimated for the simulation domain is ~19.89 m, with a maximum tsunami intrusion of ~1.12 km (Fig. 10).

Latitudinal distribution of flow depth for uniform slip scenarios fluctuates between 1.86 and 7.55 m, whereas the deterministic sources reduce the maximum observed flow depth to ~4.75 m. Meanwhile, the K–L stochastic scenarios are characterized by a wider flow depth range, between 0.07 and 24.51 m. For comparison, we included the reported maximum flow depths of the  $M_w$  8.8 1868 (~12 m) and  $M_w$  8.7 1877 (~6 m) tsunamigenic earthquakes (Soloviev and Go 1975). Although the historical data indicate a smaller event (~12 m), the proposed worst-case scenario was chosen for reasons of conservatism (Tinti et al. 2011).

The tsunami timeline starts ~12 min after the mainshock, when the first waves arrive (Tables S3 and S4) from the northeast, with an observed wave height of ~5.79 m recorded in the synthetic tide gauge IQUI\_7 (Figure S13 and Table S3) and flow depth of ~14.15 m (Table S5) near the business district and harbor facilities. The peak surface coastal current velocity is ~10.92 m/s recorded in IQUI\_2 station (Table S6) in a cross-shore sense, observed between Brava Beach and Cavancha Point. A second wave arrives ~26 min after the mainshock, reaching a significant peak wave height recorded in IQUI\_3 station (~10.55 m) (Figures S8 to S13), flow depth inundation of ~18.09 m (Table S5) and current velocity of ~10.69 m/s, recorded in IQUI\_3 station (Table S6), close to Cavancha Point. Finally, a third wave arrives ~36 min after the mainshock, when the highest tsunami flow depth (~24.51 m, Table S5) near Cavancha Cove and an extensive inundation area (~6 km<sup>2</sup>) covering almost the entire area under a topographic elevation of 30 m are observed. Additionally, two of the main observed spectral peaks (9.75 and 13.84 min) could be related to the energy impact of the first waves (Table S7).

For an extended analysis, we integrated all flow depth information generated by the stochastic scenarios for the city of Iquique to construct some sample statistics such as the mean, standard deviation, coefficient of variation and maximum. The spatial distribution of the flow depth mean fluctuates between 0 and 20 m and presents a maximum value east of Cavancha Cove (~20 m). The local business district, located near the southeast part of El Colorado beach, is affected by an extensive inundation intrusion of ~1.5 km, presenting a mean flow depth range of ~3–10 m. The section between the Serrano Peninsula and Morro Point presents a tsunami intrusion of 1 km with a mean flow depth that fluctuates

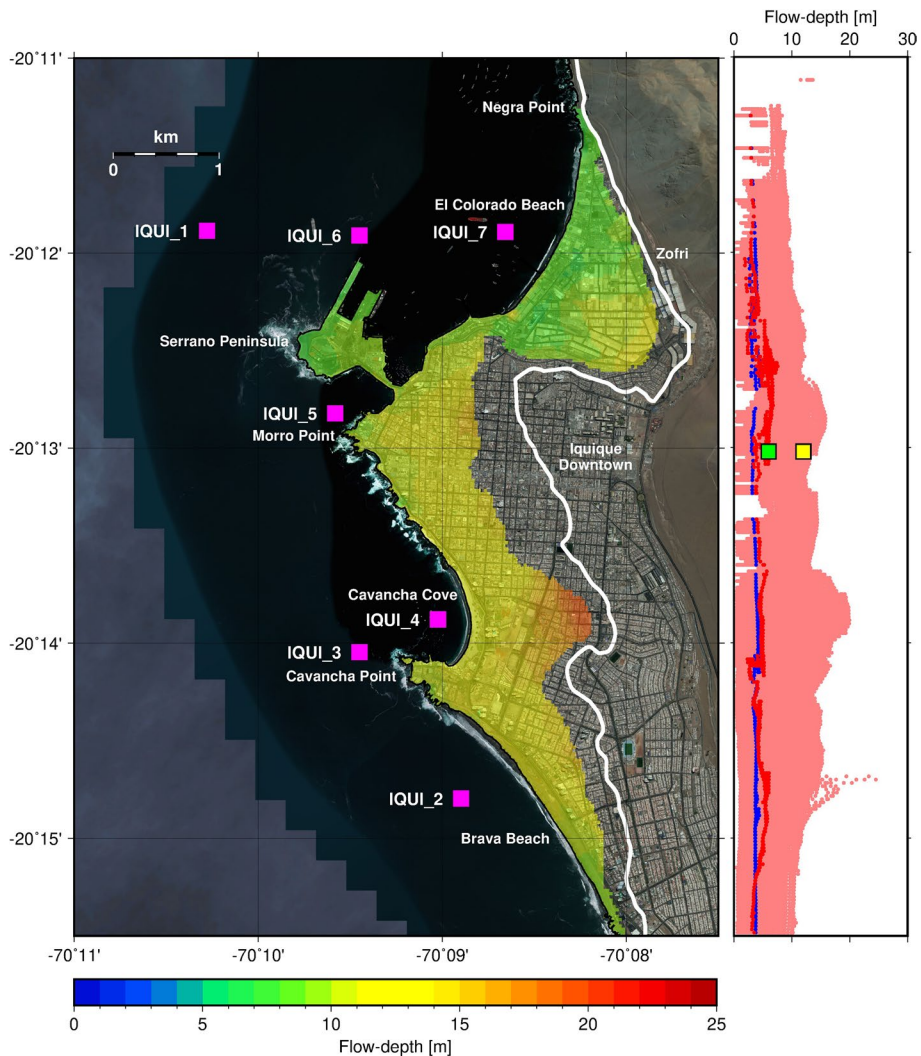


**Fig. 10** Left panel: Spatial distribution of flow depth for stochastic credible worst-case scenario modeled in Iquique, including the reported flow depths of 1868 (yellow square) and 1877 (green square). The magenta square indicates the simulated sea level records stations. Right panel: Blue and red lines denote the deterministic maximum scenario (scenario 377,  $M_w \sim 8.9$ ) and baseline homogeneous slip scenario, respectively. Pink lines show latitudinal distribution of flow depth for the 400 stochastic scenarios

from  $\sim 3$  to 15 m. On the southern sandy beaches, we observed a mean flow depth between  $\sim 3$  and 20 m and a maximum tsunami intrusion of 1 km (see Fig. 11a). The pattern of flow depth standard deviations presents a similar behavior, with a range of  $\sim 0$ –2 m. The lowest range of variation is an important value for the design of vertical evacuation infrastructure and tsunami evacuation routes. For example, we found that there is a specific site with a low range variation on the Serrano Peninsula, which is a potential location for vertical evacuation sites due to the possibility that the peninsula could become an island during a

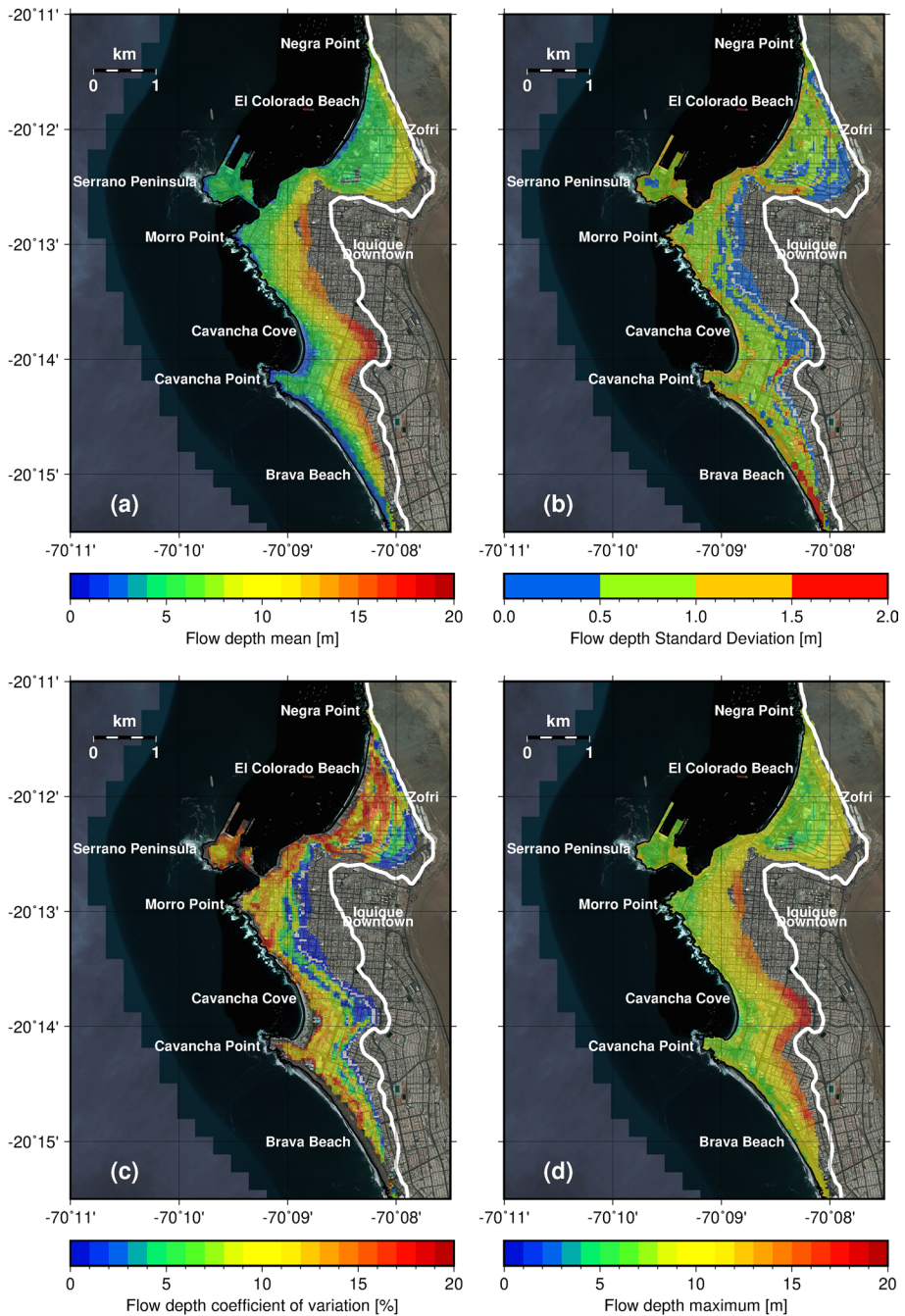


**Fig. 11** Spatial distribution of flow depth **a** mean, **b** standard deviation, **c** coefficient of variation and **d** maximum estimated based on tsunami inundation of all stochastic scenarios modeled in Iquique



tsunami event (see Fig. 11b). The flow depth coefficient of variation is the ratio between the standard deviation and the mean and is useful for evaluating the homogeneity or low dispersion of the data; it can be represented by a percentage. A homogeneous system can be represented by a coefficient of variation under 2%. The level of the lowest dispersion of flow depth data can be found in the southeast section of the business district and in the easternmost area of the south central coastal segment (see Fig. 11c). The spatial distribution of the flow depth maximum fluctuates between ~4 and 20 m, with a maximum in the eastern section of the southern sandy beaches (see Fig. 11d).

Finally, based on the Aki–Utsu estimator methodology applied to the historical earthquake catalog, we obtained the recurrence time in years and the probability of occurrence for a subset of magnitudes ( $8.0 \geq M_w \geq 9.1$ ) derived from the stochastic rupture scenario analysis. The estimated credible worst-case scenario in Iquique is a  $M_w \sim 8.9$  event that produces a tsunami flow depth of 24.51 m, with a referential earthquake recurrence time of 395 years (Table S8).

## 4 Discussion

We used a semiquantitative approach to define a set of deterministic scenarios from relevant geophysical parameters, e.g., trench-parallel gravity anomalies, interseismic coupling distribution and historical and instrumental seismicity. The tsunamigenic sources calculated in this way exhibited a heterogeneous slip-deficit pattern, which is an improvement over the classical use of uniform slip sources for tsunami hazard assessment. Nevertheless, the use of slip-deficit deterministic sources in tsunami numerical models revealed a systematic underestimation of wave height, inundation area and flow depth, which ended up being comparable to those from uniform slip ruptures. While this slip-deficit approach has been used elsewhere, such as Watanabe et al. (2018), our results led us to question the validity or usefulness of slip-deficit sources to predict realistic impacts of future events. Thus, while our deterministic approach is an improvement, it clearly underestimates the coastal impacts of tsunamis based on records of historical earthquakes in the seismic gap (Milne 1880; Vidal Gormaz 1878). The failure of the slip-deficit sources can be attributed to the transient nature of interseismic coupling (Loveless and Meade 2016; Nishimura et al. 2004). Furthermore, whether large events release the entirety of the accumulated slip deficit or some deficit can persist between earthquake cycles is not known. All of these factors will invariably lead to an underestimation of the maximum peak slip of a seismic scenario (Métois et al. 2016).

Recently, the conventional asperity scheme provided by Lay and Kanamori (1981) has been improved using a categorization of global large megathrust earthquake rupture complexity (Ye et al. 2018). Based on the rupture complexity criterion, the southern Peru and northern Chile segment can be characterized by rough asperity patches, large interpatch separation, heterogeneous coupling and patch interaction prone to earthquake triggering. However, the modified asperity model proposed by Ye et al. (2018) can schematize the analyzed segment with only two main patches with  $M_w$  8.6 for a single rupture and  $M_w$  8.8 for a combined rupture, differing from our proposal of four asperity occurrences.

The aforementioned weakness of deterministic approaches can be overcome by employing a stochastic method to generate non-uniform slip distributions. In this work, the K–L expansion method (LeVeque et al. 2016; Melgar et al. 2016) leads to a wider variability of the maximum peak slip and distribution of the asperities in the scenarios. Furthermore, as also noted

by Li et al. (2016), this wide variability of seismic behaviors in modeled scenarios constitutes a powerful tool to evaluate the uncertainty of coastal tsunami data (Melgar et al. 2016). An important characteristic of the technique is the presence of extreme events in the scenario rupture catalog. For example, the scenario 380 ( $M_w$  9.2) exhibits a single asperity that releases an extreme peak slip of  $\sim 39.89$  m, concentrated along  $\sim 200$  km of the rupture length. Meanwhile, the scenario 392 ( $M_w$  8.9) presents a broad spatial length of  $\sim 542$  km and a small value of slip released ( $\sim 18.23$  m). The specific characteristics of the selected scenarios illustrate the wide range of seismic behaviors in the rupture catalog, generating high variability and uncertainties in tsunami hazard assessment (Sepúlveda et al. 2017).

In order to improve the computation time needed to construct a robust scenario database, a finite number of tsunamigenic scenarios must be analyzed. According to statistical tests, we defined the minimum number of scenarios (400) needed to maintain the variability of our target population of 20,000 scenarios. For subsequent analysis, the stability of the variation coefficient applied to an exhaustive simulation database needs to be explored. The preliminary approach using the minimum number of scenarios is capable of providing a simplified view of the uncertainty in the hydrodynamic variables associated with the coastal impact of tsunamis.

The southern Peru and northern Chile seismic gap has been affected by two major tsunamigenic earthquakes in the last 150 years, which caused substantial damage in coastal cities such as Arica, Iquique, Tocopilla, Cobija and Mejillones. In the city of Iquique, the tsunami associated with the 1868  $M_w$  8.8 earthquake (Dorbath et al. 1990) generated a maximum tsunami inundation height of  $\sim 12$  m and an extensive inundation area in the lower coastal zone near downtown (Soloviev and Go 1975). To validate the reported flow depth, values of this event can be compared with the stochastic scenario flow depth database. The spatial distribution of the flow depth mean ranged from  $\sim 4$  to 12 m in the city's historical downtown, located approximately between Negra and Morro points. Other relevant reported information is the tsunami waves speed of 7 m/s (Soloviev and Go 1975), comparable to our results for the maximum scenario of  $\sim 10.92$  m/s.

The empirical relationship observed between the maximum flow depth and peak slip presents a non-strong causative effect of a complex seismic source, opposed to findings reported by Geist (2002), mainly due to the flow depth calculation under breaking wave conditions. Most stochastic scenarios ( $\sim 81\%$ ) present a peak slip that fluctuates between 1.24 and 20 m, with a high percentage ( $\sim 95\%$ ) of flow depths less than 10 m. Extreme flow depth values over  $\sim 20$  m can be associated with peak slips ranging between 20 and 40 m ( $M_w \geq 8.5$ ). The scattering in the linear scaling could be related to the morphological effects of steep topographic gradients or harbor resonance processes.

The broad diversity of the stochastic seismic scenarios, presenting wide ranges of magnitudes and peak slip, can be useful for evaluating local effects using detailed inundation modeling, e.g., arrival time of tsunami waves for different scenarios (Figure S14). Furthermore, our comprehensive scenario database provides an initial multi-scenario tsunami hazard assessment, which, along with other considerations inherent to the risk analysis, can be useful for evaluating evacuation zoning, land-use planning and design of vertical evacuation structures.

## 5 Summary and conclusions

In this paper, we proposed a hybrid deterministic and stochastic approach to define the seismogenic potential of a mature seismic gap in southern Peru and northern Chile and subsequently perform a scenario-based tsunami hazard assessment of coastal

settlements. Initially, based on gravity models, instrumental seismicity and slip deficit derived from geodetic locking models, we defined a preliminary structure scheme of the main asperities and the maximum earthquakes associated with them. The tsunami simulation of these deterministic scenarios fails to match the historical flow depth reported in the city of Iquique, systematically underestimating it. To overcome this limitation, we adapted a novel stochastic technique based on the Karhunen–Loève (K–L) expansion to generate a database of rupture scenarios, including constrained fault geometry and reasonable restrictions on the maximum slip. Then, a data set of 400 stochastic scenarios was defined as the input for tsunami modeling performed using NEOWAVE. Finally, we obtained a database of tsunami wave heights, inundation extent, flow depth, arrival times and spectral energy. Here, we focused on the tsunami threat for the city of Iquique as a case study. The relationship between the maximum flow depth and peak slip shows that a complex source acts as a non-strong control on tsunami inundation, if we consider a wave breaking regime, with heterogeneous slip being a second-order control on the flow depth pattern during the inundation, compared to other factors affecting the hydrodynamic processes of inundation such as resonance and local morphology (Cortés et al. 2017; Ezersky et al. 2013). Opposite findings in Iquique have been reported by Sepúlveda et al. (2017), but considering a non-breaking wave regime.

The temporal evolution of the tsunami waves generated by the credible worst-case earthquake scenario in Iquique can be characterized by the impact of at least three main wave trains, with an initial arrival time of  $\sim 12$  min after the mainshock. The maximum wave height, tsunami flow depth and horizontal intrusion occur the northern area of the city, close to business district and harbor facilities, and in the central section near Cavancha Cove, an important area for tourism. The maximum flow depth area is  $\sim 6$  km<sup>2</sup>, covering nearly all the coastal areas below the safety line ( $\sim 30$  m elevation). The calculated spectral peak of  $\sim 13.84$  min has been reported by Cortés et al. (2017), indicating a reasonable simulation of coastal resonance processes.

The integration of complete flow depth information using sample statistics can be useful for determining evacuation protocols and the geographical locations of safe zones. For example, for the stochastic scenario database the maximum flow depth never exceeds the topographic level of 30 m, making this level suitable for demarcating the safe zone. Moreover, the combination of different sample statistics such as mean, standard deviation and coefficient of variation provides information for the design of evacuation routes and vertical evacuation buildings.

**Acknowledgements** This research has been funded by a Ph.D. scholarship awarded by Universidad Católica del Norte, Antofagasta, and the CONICYT FONDAP Program through Grant No. 1511017. We acknowledge the National Hydrographic and Oceanographic Service of the Chilean Navy for providing the local topography and bathymetric database used in the tsunami simulations. LIDAR high-resolution topography for Iquique was acquired through the JICA-JST SATREPS tsunami collaboration project, “Enhancement of Technology to Develop Tsunami-Resilient Community,” between Chile and Japan. Global bathymetry data were extracted from GEBCO (<http://www.gebco.net>). Intensive tsunami modeling was supported by the supercomputing infrastructure of the National Laboratory for High Performance Computing (NLHPC/ECM-02) and the technical support of Mr. Diego Urrutia (Department of System and Computation Engineering, Universidad Católica del Norte, Antofagasta). We are thankful to Dr. Gonzalo Yáñez (Engineering School, Pontificia Universidad Católica de Chile, Santiago) for introducing the trench-parallel gravity anomaly (TPGA) methodology. Our acknowledgements to Dr. Roberto Benavente (Department of Civil Engineering, Universidad Católica de la Santísima Concepción) and Mr. Alejandro Urrutia (Research Center for Integrated Disaster Risk Management) for the valuable and fruitful comments. N. Zamora has been funded by the Fondecyt No. 3170895. Research funding for M.N. Shrivastava was provided by Fondecyt No. 3160773.

## References

- Aguirre P, Vásquez J, de la Llera JC, González J, González G (2018) Earthquake damage assessment for deterministic scenarios in Iquique, Chile. *Nat Hazards* 92(3):1433–1461. <https://doi.org/10.1007/s11069-018-3258-3>
- Aki K (1965) Maximum Likelihood estimate of  $b$  in the formula  $\log N = a - bM$  and its confidence limits. *Bull Earthq Res Inst* 43:237–239
- Allen TI, Hayes GP (2017) Alternative rupture-scaling relationships for subduction interface and other off-shore environments. *Bull Seismol Soc Am* 107(3):1240–1253. <https://doi.org/10.1785/0120160255>
- An C, Liu PLF (2014) Characteristics of leading tsunami waves generated in three recent tsunami events. *J Earthq Tsunami* 8(3):1440001. <https://doi.org/10.1142/S1793431114400016>
- Aránguiz R, González G, González J, Catalán PA, Cienfuegos R, Yagi Y, Okuwaki R, Urra L, Contreras K, Del Río I, Rojas C (2016) The 16 September 2015 Chile tsunami from the post-tsunami survey and numerical modeling perspectives. *Pure Appl Geophys* 173(2):333–348. <https://doi.org/10.1007/s00024-015-1225-4>
- Argus DF, Gordon RG, Heflin MB, Ma C, Eanes RJ, Willis P, Peltier WR, Owen SE (2010) The angular velocities of the plates and the velocity of Earth's centre from space geodesy. *Geophys J Int* 180(3):913–960. <https://doi.org/10.1111/j.1365-246X.2009.04463.x>
- Bai Y, Cheung KF, Yamazaki Y, Lay T, Ye L (2014) Tsunami surges around the Hawaiian Islands from the 1 April 2014 North Chile Mw 8.1 earthquake. *Geophys Res Lett* 41(23):8512–8521. <https://doi.org/10.1002/2014GL061686>
- Béjar-Pizarro M, Carrizo D, Socquet A, Armijo R, Barrientos S, Bondoux F, Bonvalot S, Campos J, Comte D, De Chabaliér JB, Charade O, Delorme A, Gabalda G, Galetzka J, Genrich J, Nercessian A, Olcay M, Ortega F, Ortega I, Remy D, Ruegg JC, Simons M, Valderas C, Vigny C (2010) Asperities and barriers on the seismogenic zone in North Chile: state-of-the-art after the 2007 Mw 7.7 Tocopilla earthquake inferred by GPS and InSAR data. *Geophys J Int* 183(1):390–406. <https://doi.org/10.1111/j.1365-246X.2010.04748.x>
- Blaser L, Krüger F, Ohrnberger M, Scherbaum F (2010) Scaling relations of earthquake source parameter estimates with special focus on subduction environment. *Bull Seismol Soc Am* 100(6):2914–2926. <https://doi.org/10.1785/0120100111>
- Catalán PA, Aránguiz R, González G, Tomita T, Cienfuegos R, González J, Shrivastava MN, Kumagai K, Mokrani C, Cortés P, Gubler A (2015) The 1 April 2014 Pisagua tsunami: observations and modeling. *Geophys Res Lett* 42(8):2918–2925. <https://doi.org/10.1002/2015GL063333>
- Cheung KF, Wei Y, Yamazaki Y, Yim SC (2011) Modeling of 500-year tsunamis for probabilistic design of coastal infrastructure in the Pacific Northwest. *Coast Eng* 58(10):970–985. <https://doi.org/10.1016/j.coastaleng.2011.05.003>
- Cheung KF, Bai Y, Yamazaki Y (2013) Surges around the Hawaiian Islands from the 2011 Tohoku Tsunami. *J Geophys Res Oceans* 118(10):5703–5719. <https://doi.org/10.1002/jgrc.20413>
- Chlieh M, Avouac JP, Hjorleifsdottir V, Song TRA, Ji C, Sieh K, Sladen A, Hebert H, Prawirodirdjo L, Bock Y, Galetzka J (2007) Coseismic slip and afterslip of the great Mw 9.15 Sumatra–Andaman earthquake of 2004. *Bull Seismol Soc Am* 97(1A):S152–S173. <https://doi.org/10.1785/0120050631>
- Chlieh M, Perfettini H, Tavera H, Avouac JP, Remy D, Nocquet JM, Rolandone F, Bondoux F, Gabalda G, Bonvalot S (2011) Interseismic coupling and seismic potential along the Central Andes subduction zone. *J Geophys Res* 116(B12):1–21. <https://doi.org/10.1029/2010JB008166>
- Comte D, Pardo M (1991) Reappraisal of great historical earthquakes in the northern Chile and southern Peru seismic gaps. *Nat Hazards* 4(1):23–44. <https://doi.org/10.1007/BF00126557>
- Cortés P, Catalán PA, Aránguiz R, Bellotti G (2017) Tsunami and shelf resonance on northern Chile coast. *J Geophys Res Oceans* 122(9):7364–7379
- Das R, Wason HR, Gonzalez G, Sharma ML, Choudhury D, Lindholm C, Roy N, Salazar P (2018) Earthquake magnitude conversion problem. *Bull Seismol Soc Am* 108(4):1995–2007. <https://doi.org/10.1785/0120170157>
- Delouis B, Monfret T, Dorbath L, Pardo M, Rivera L, Comte D, Haessler H, Caminade JP, Ponce L, Kausel E, Cisternas A (1997) The Mw = 8.0 Antofagasta (northern Chile) earthquake of 30 July 1995: a precursor to the end of the large 1877 gap. *Bull Seismol Soc Am* 87(2):427–445
- Dorbath L, Cisternas A, Dorbath C (1990) Assessment of the size of large and great historical earthquakes in Peru. *Bull Seismol Soc Am* 80(3):551–576
- Ezersky A, Tiguercha D, Pelinovsky E (2013) Resonance phenomena at the long wave run-up on the coast. *Nat Hazards Earth Syst Sci* 13(11):2745–2752. <https://doi.org/10.5194/nhess-13-2745-2013>
- Farr T, Rosen PA, Caro E, Crippen R, Duren R, Hensley S, Kobrick M, Paller M, Rodriguez E, Roth L, Seal D, Shaffer S, Shimada J, Umland J, Werner M, Oskin M, Burbank D, Alsdorf D (2007) The shuttle

- radar topography mission. *Rev Geophys* 45(2):1–33. <https://doi.org/10.1029/2005RG000183.1>. **INTRODUCTION**
- Fletcher HJ, Beavan J, Freymueller JT, Gilbert L (2001) High interseismic coupling of the Alaska subduction zone SW of Kodiak island inferred from GPS data. *Geophys Res Lett* 28(3):443–446
- Frigo M, Johnson SG (1998) FFTW: an adaptive software architecture for the FFT. In: ICASSP, IEEE international conference on acoustics, speech and signal processing—proceedings, vol 3, pp 1381–1384. <https://doi.org/10.1109/ICASSP.1998.681704>
- Geist EL (1998) Local tsunamis and earthquake source parameters. *Adv Geophys* 39:117–209
- Geist EL (2002) Complex earthquake rupture and local tsunamis. *J Geophys Res* 107(B5):1–16. <https://doi.org/10.1029/2000JB000139/full>
- Geist EL, Dmowska R (1999) Local tsunamis and distributed slip at the source. *Pure Appl Geophys* 154:485–512. [https://doi.org/10.1007/978-3-0348-8679-6\\_6](https://doi.org/10.1007/978-3-0348-8679-6_6)
- Guibourg S, Heinrich P, Roche R (1997) Numerical modeling of the 1995 Chilean tsunami. Impact on French Polynesia. *Geophys Res Lett* 24(7):775–778
- Gutenberg B, Richter CF (1944) Frequency of earthquakes in California. *Bull Seismol Soc Am* 34(4):185–188
- Hayes GP (2017) The finite, kinematic rupture properties of great-sized earthquakes since 1990. *Earth Planet Sci Lett* 468:94–100. <https://doi.org/10.1016/j.epsl.2017.04.003>
- Hayes GP, Wald DJ, Johnson RL (2012) Slab1.0: a three-dimensional model of global subduction zone geometries. *J Geophys Res* 117(B1):1–15. <https://doi.org/10.1029/2011JB008524>
- Hayes GP, Herman MW, Barnhart WD, Furlong KP, Riquelme S, Benz HM, Bergman E, Barrientos S, Earle PS, Samsonov SV (2014) Continuing megathrust earthquake potential in Chile after the 2014 Iquique earthquake. *Nature* 512(7514):295–299. <https://doi.org/10.1038/nature13677>
- Heidarzadeh M, Satake K (2014) Excitation of basin-wide modes of the Pacific ocean following the March 2011 Tohoku tsunami. *Pure Appl Geophys* 171(12):3405–3419. <https://doi.org/10.1007/s00024-013-0731-5>
- Heidarzadeh M, Satake K, Murotani S, Gusman AR, Watada S (2015) Deep-water characteristics of the trans-Pacific tsunami from the 1 April 2014 Mw 8.2 Iquique, Chile Earthquake. *Pure Appl Geophys* 172(3–4):719–730. <https://doi.org/10.1007/s00024-014-0983-8>
- Hoffmann F, Metzger S, Moreno M, Deng Z, Sippl C, Ortega-Culaciati F, Oncken O (2018) Characterizing afterslip and ground displacement rate increase following the 2014 Iquique-Pisagua Mw 8.1 earthquake, Northern Chile. *J Geophys Res Solid Earth*. <https://doi.org/10.1002/2017JB014970>
- Kelleher JA (1972) Rupture zones of large South American earthquakes and some predictions. *J Geophys Res* 77(11):2087. <https://doi.org/10.1029/JB077i011p02087>
- Kijko A, Smit A (2012) Extension of the Aki–Utsu b-Value estimator for incomplete catalogs. *Bull Seismol Soc Am* 102(3):1283–1287. <https://doi.org/10.1785/0120110226>
- Lay T, Kanamori H (1981) An asperity model of large earthquake sequences. *Earthq Predict* 4:579–592. <https://doi.org/10.1029/ME004p0579>
- Lay T, Ye L, Kanamori H, Yamazaki Y, Cheung KF, Ammon CJ (2013) The February 6, 2013 Mw 8.0 Santa Cruz Islands earthquake and tsunami. *Tectonophysics* 608:1109–1121. <https://doi.org/10.1016/j.tecto.2013.07.001>
- LeVeque RJ, Waagan K, González FI, Rim D, Lin G (2016) Generating random earthquake events for probabilistic tsunami hazard assessment. *Pure Appl Geophys* 173(12):3671–3692. <https://doi.org/10.1007/s00024-016-1357-1>
- Li L, Switzer AD, Chan CH, Wang Y, Weiss R, Qiu Q (2016) How heterogeneous coseismic slip affects regional probabilistic tsunami hazard assessment: a case study in the South China Sea. *J Geophys Res Solid Earth* 121(8):6250–6272. <https://doi.org/10.1002/2016JB013111>
- Lomnitz C (2004) Major earthquakes of Chile: a historical survey, 1535–1960. *Seismol Res Lett* 75(3):368–378
- Lorito S, Romano F, Atzori S, Tong X, Avallone A, McCloskey J, Cocco M, Boschi E, Piatanesi A (2011) Limited overlap between the seismic gap and coseismic slip of the great 2010 Chile earthquake. *Nat Geosci* 4(3):173–177. <https://doi.org/10.1038/ngeo1073>
- Loveless JP, Meade BJ (2016) Two decades of spatiotemporal variations in subduction zone coupling off-shore Japan. *Earth Planet Sci Lett* 436:19–30. <https://doi.org/10.1016/j.epsl.2015.12.033>
- Mai PM, Thingbaijam KKS (2014) SRCMOD: an online database of finite-fault rupture models. *Seismol Res Lett* 85(6):1348–1357. <https://doi.org/10.1785/0220140077>
- McCann WR, Nishenko SP, Sykes LR, Krause J (1979) Seismic gaps and plate tectonics: seismic potential for major boundaries. *Pure Appl Geophys* 117(6):1082–1147. [https://doi.org/10.1007/978-3-0348-6430-5\\_2](https://doi.org/10.1007/978-3-0348-6430-5_2)


- Melgar D, Ruiz-Angulo A (2018) Long-lived tsunami edge waves and shelf resonance from the M8.2 Tehuantepec earthquake. *Geophys Res Lett* 45:12414–12421. <https://doi.org/10.1029/2018GL080823>
- Melgar D, LeVeque RJ, Dreger DS, Allen RM (2016) Kinematic rupture scenarios and synthetic displacement data: an example application to the Cascadia subduction zone. *J Geophys Res Solid Earth* 121(9):6658–6674. <https://doi.org/10.1002/2016JB013314>
- Métouis M, Socquet A, Vigny C, Carrizo D, Peyrat S, Delorme A, Maureira E, Valderas-Bermejo MC, Ortega I (2013) Revisiting the north Chile seismic gap segmentation using GPS-derived interseismic coupling. *Geophys J Int* 194(3):1283–1294. <https://doi.org/10.1093/gji/ggt183>
- Métouis M, Vigny C, Socquet A (2016) Interseismic coupling, megathrust earthquakes and seismic swarms along the Chilean subduction zone (38°–18°S). *Pure Appl Geophys* 173(5):1431–1449. <https://doi.org/10.1007/s00024-016-1280-5>
- Michael AJ (1990) Energy constraints on kinematic models of oblique faulting: Loma Prieta versus Parkfield-Coalinga. *Geophys Res Lett* 17(9):1453–1456. <https://doi.org/10.1029/GL017i009p01453>
- Milne A (1880) The Peruvian earthquake of 9th May, 1877. *Trans Seismol Soc Jpn* 2:50–96
- Mueller C, Power WL, Fraser XL, Wang X (2015) Effects of rupture complexity on local tsunami inundation: implications for probabilistic tsunami hazard assessment by example. *J Geophys Res Solid Earth* 120(1):488–502. <https://doi.org/10.1002/2014JB011301>
- Nishenko SP (1985) Seismic potential for large and great interplate earthquakes along the Chilean and southern Peruvian margins of South America: a quantitative reappraisal. *J Geophys Res* 90(B5):3589–3615. <https://doi.org/10.1029/JB090iB05p03589/full>
- Nishimura T, Hirasawa T, Miyazaki SI, Sagiya T, Tada T, Miura S, Tanaka K (2004) Temporal change of interplate coupling in northeastern Japan during 1995–2002 estimated from continuous GPS observations. *Geophys J Int* 157(2):901–916. <https://doi.org/10.1111/j.1365-246X.2004.02159.x>
- Okal EA, Dengler LA, Araya S, Borrero JC, Gomer BM, Koshimura S, Laos G, Olcese D, Ortiz F, Swenson M, Titov VV, Vegas F (2002) Field survey of the Camaná, Perú tsunami of 23 June 2001. *Seismol Res Lett* 73(6):907–920
- Okal EA, Borrero JC, Synolakis CE (2006) Evaluation of tsunami risk from regional earthquakes at Pisco, Peru. *Bull Seismol Soc Am* 96(5):1634–1648. <https://doi.org/10.1785/0120050158>
- Oleskevich DA, Hyndman RD, Wang K (1999) The updip and downdip limits to great subduction earthquakes: thermal and structural models of Cascadia, south Alaska, SW Japan, and Chile. *J Geophys Res* 104(B7):14965–14991. <https://doi.org/10.1029/1999JB900060/full>
- Peyrat S, Madariaga R, Buforn E, Campos J, Asch G, Vilotte JP (2010) Kinematic rupture process of the 2007 Tocopilla earthquake and its main aftershocks from teleseismic and strong-motion data. *Geophys J Int* 182(3):1411–1430. <https://doi.org/10.1111/j.1365-246X.2010.04685.x>
- Piatanesi A, Lorito S (2007) Rupture process of the 2004 Sumatra–Andaman earthquake from tsunami waveform inversion. *Bull Seismol Soc Am* 97(1):223–231. <https://doi.org/10.1785/0120050627>
- Plafker G (1997) Catastrophic tsunami generated by submarine slides and backarc thrusting during the 1992 earthquake on eastern Flores I., Indonesia. In: Geological Society of America, Cordilleran Section, 93rd Annual Meeting, vol 29, p 57
- Pollitz FF, Bürgmann R, Banerjee P (2011) Geodetic slip model of the 2011 M9.0 Tohoku earthquake. *Geophys Res Lett* 38(7):1–6. <https://doi.org/10.1029/2011GL048632>
- Rosenau M, Nerlich R, Brune S, Oncken O (2010) Experimental insights into the scaling and variability of local tsunamis triggered by giant subduction megathrust earthquakes. *J Geophys Res Solid Earth* 115(9):1–20. <https://doi.org/10.1029/2009JB007100>
- Ruegg JC, Olcay M, Lazo D (2001) Co-, post- and pre(?)–seismic displacements associated with the Mw 8.4 Southern Peru earthquake of 23 June 2001 from continuous GPS measurements. *Seismol Res Lett* 72(6):673–678
- Ruiz S, Madariaga R (2018) Historical and recent large megathrust earthquakes in Chile. *Tectonophysics* 733:37–56. <https://doi.org/10.1016/j.tecto.2018.01.015>
- Ruiz JA, Fuentes MA, Riquelme S, Campos J, Cisternas A (2015) Numerical simulation of tsunami runup in northern Chile based on non-uniform k 22 slip distributions. *Nat Hazards* 79(2):1177–1198. <https://doi.org/10.1007/s11069-015-1901-9>
- Sandwell DT, Müller RD, Smith WHF, Garcia ES, Francis R (2014) New global marine gravity model from CryoSat-2 and Jason-1 reveals buried tectonic structure. *Science* 346(6205):65–67. <https://doi.org/10.1126/science.1258213>
- Scholz CH, Campos J (2012) The seismic coupling of subduction zones revisited. *J Geophys Res* 117(B5):1–22. <https://doi.org/10.1029/2011JB009003>
- Schurr B, Asch G, Hainzl S, Bedford J, Hoechner A, Palo M, Wang R, Moreno M, Bartsch M, Zhang Y, Oncken O, Tilmann F, Dahm T, Victor P, Barrientos S, Vilotte JP (2014) Gradual unlocking of plate boundary controlled initiation of the 2014 Iquique earthquake. *Nature* 512(7514):299–311. <https://doi.org/10.1038/nature13681>



- Seno T (2014) Stress drop as a criterion to differentiate subduction zones where Mw 9 earthquakes can occur. *Tectonophysics* 621:198–210. <https://doi.org/10.1016/j.tecto.2014.02.016>
- Sepúlveda I, Liu PLF, Grigoriu M, Pritchard ME (2017) Tsunami hazard assessments with consideration of uncertain earthquake slip distribution and location. *J Geophys Res Solid Earth* 122(9):7252–7271. <https://doi.org/10.1002/2017JB014430>
- Shrivastava MN, González G, Moreno M, Soto H, Schurr B, Salazar P, Báez JC (2019) Earthquake segmentation in northern Chile correlates with curved plate geometry. *Sci Rep* 9(1):1–10. <https://doi.org/10.1038/s41598-019-40282-6>
- Simons M, Minson SE, Sladen A, Ortega-Culaciati F, Jiang J, Owen SE, Meng L, Ampuero JP, Wei S, Chu R, Helmlinger DV, Webb FH (2011) The 2011 magnitude 9.0 Tohoku-Oki earthquake: mosaicking the megathrust from seconds to centuries. *Science* 332(6036):1421–1425. <https://doi.org/10.1126/science.1206731>
- Smith WHF, Wessel P (1990) Gridding with continuous curvature splines in tension. *Geophysics* 55(3):293–305. <https://doi.org/10.1190/1.1442837>
- Sobiesiak M, Meyer U, Schmidt S, Götz HJ, Krawczyk CM (2007) Asperity generating upper crustal sources revealed by b value and isostatic residual anomaly grids in the area of Antofagasta, Chile. *J Geophys Res* 112(B12):1–11. <https://doi.org/10.1029/2006JB004796>
- Soloviev SL, Go CN (1975) A catalogue of tsunamis on the eastern shore of the Pacific Ocean (1513–1968). *Can Transl Fish Aquat Sci* 5078(1984):1–294
- Song TRA, Simons M (2003) Large trench-parallel gravity variations predict seismogenic behavior in subduction zones. *Science* 301(5633):630–633
- Tavera H, Buforn E, Bernal I, Antayhua Y, Vilacapoma L (2002) The Arequipa (Peru) earthquake of June 23, 2001. *J Seismol* 6(2):279–283. <https://doi.org/10.1023/A:1015698621075>
- Tinti S, Tonini R, Bressan L, Armigliato AC, Gardi A, Guillande R, Valencia N, Scheer S (2011) Handbook of tsunami hazard and damage scenarios. JRC Sci Tech Rep. <https://doi.org/10.2788/21259>
- Vidal Gormaz F (1878) Algunos datos relativos al terremoto de 9 de mayo de 1877, i a las agitaciones del mar i de los otros fenómenos ocurridos sobre las costas occidentales de Sud-América. *Anuario Hidrográfico de Chile* 4:458–480
- Vigny C, Socquet A, Peyrat S, Ruegg JC, Métois M, Madariaga R, Morvan S, Lancieri M, Lacassin R, Campos J, Carrizo D, Bejar-Pizarro M, Barrientos S, Armijo R, Aranda C, Valderas-Bermejo MC, Ortega I, Bondoux F, Baize S, Lyon-Caen H, Pavez A, Vilotte JP, Bevis M, Brooks B, Smalley R, Parra H, Baez JC, Blanco M, Cimbaro S, Kendrick EC (2011) The 2010 Mw 8.8 Maule megathrust earthquake of Central Chile, monitored by GPS. *Science* 332(6036):1417–1421. <https://doi.org/10.1126/science.1204132>
- Villegas-Lanza JC, Chlieh M, Cavalié O, Tavera H, Baby P, Chire J, Nocquet JM (2016) Active tectonics of Peru: heterogeneous interseismic coupling along the Nazca Megathrust, rigid motion of the Peruvian Sliver and Subandean shortening accommodation. *J Geophys Res Solid Earth* 121(10):7371–7394. <https://doi.org/10.1002/2016JB013080>
- Watanabe S, Bock Y, Melgar D, Tadokoro K (2018) Tsunami scenarios based on interseismic models along the Nankai Trough, Japan from seafloor and onshore geodesy. *J Geophys Res Solid Earth* 123(3):2448–2461. <https://doi.org/10.1002/2017JB014799>
- Weatherall P, Marks KM, Jakobsson M, Schmitt T, Tani S, Arndt JE, Rovere M, Chayes D, Ferrini V, Wigley R (2015) A new digital bathymetric model of the world's oceans. *Earth Space Sci* 2(8):331–345. <https://doi.org/10.1002/2015EA000107>
- Weichert DH (1980) Estimation of the earthquake recurrence parameters for unequal observation periods for different magnitudes. *Bull Seismol Soc Am* 70(4):1337–1346. <https://doi.org/10.1017/CBO9781107415324.004>
- Welch BL (1951) On the comparison of several mean values: an alternative approach. *Biometrika* 38(3–4):330–336. <https://doi.org/10.2307/2332579>
- Wessel P, Smith WHF (2013) Generic mapping tools: improved version released. *EOS Trans* 94(45):409–410
- Yamazaki Y, Cheung KF (2011) Shelf resonance and impact of near-field tsunami generated by the 2010 Chile earthquake. *Geophys Res Lett* 38(L12):1–8. <https://doi.org/10.1029/2011GL047508>
- Yamazaki Y, Cheung KF, Kowalik Z (2011) Depth-integrated, non-hydrostatic model with grid nesting for tsunami generation, propagation, and run-up. *Int J Numer Methods Fluids* 61(5):473–497. <https://doi.org/10.1002/fld>
- Yamazaki Y, Cheung KF, Lay T (2013) Modeling of the 2011 Tohoku Near-Field Tsunami from Finite-Fault Inversion of Seismic Waves. *Bull Seismol Soc Am* 103(2B):1444–1455. <https://doi.org/10.1785/0120120103>
- Ye L, Kanamori H, Lay T (2018) Global variations of large megathrust earthquake rupture characteristics. *Sci Adv* 4(3):1–7

**Publisher's Note** Springer Nature remains neutral with regard to jurisdictional claims in published maps and institutional affiliations.

## Affiliations

**Juan González**<sup>1,2</sup>  · **Gabriel González**<sup>1,2</sup> · **Rafael Aránguiz**<sup>1,3</sup> · **Diego Melgar**<sup>4</sup> · **Natalia Zamora**<sup>1,5,8</sup> · **Mahesh N. Shrivastava**<sup>1,2</sup> · **Ranjit Das**<sup>1,2</sup> · **Patricio A. Catalán**<sup>1,5,6</sup> · **Rodrigo Cienfuegos**<sup>1,7</sup>

✉ Juan González  
jgonzal@alumnos.ucn.cl

<sup>1</sup> Centro de Investigación para la Gestión Integrada del Riesgo de Desastres CONICYT FONDAP 1511007 (CIGIDEN), Santiago, Chile

<sup>2</sup> Departamento de Ciencias Geológicas, Universidad Católica del Norte, Antofagasta, Chile

<sup>3</sup> Departamento de Ingeniería Civil, Universidad Católica de la Santísima Concepción, Concepción, Chile

<sup>4</sup> Department of Earth Sciences, University of Oregon, Eugene, OR, USA

<sup>5</sup> Departamento de Obras Civiles, Universidad Técnica Federico Santa María, Valparaíso, Chile

<sup>6</sup> Centro Científico Tecnológico de Valparaíso (CCTVal), Universidad Técnica Federico Santa María, Valparaíso, Chile

<sup>7</sup> Departamento de Ingeniería Hidráulica y Ambiental, Pontificia Universidad Católica de Chile, Santiago, Chile

<sup>8</sup> CYCLO Millennium Nucleus, The Seismic Cycle Along Subduction Zones, Valdivia, Chile